

See discussions, stats, and author profiles for this publication at: <https://www.researchgate.net/publication/268792567>

# Evaporation Assisted CdSe Nanorod Assembly by Small Angle X-ray Scattering and Langmuir Adsorption

ARTICLE *in* THE JOURNAL OF PHYSICAL CHEMISTRY B · NOVEMBER 2014

Impact Factor: 3.3 · DOI: 10.1021/jp508548q · Source: PubMed

---

READS

15

## 1 AUTHOR:



**Kimani Stancil**

U.S. Merchant Marine Academy

9 PUBLICATIONS 258 CITATIONS

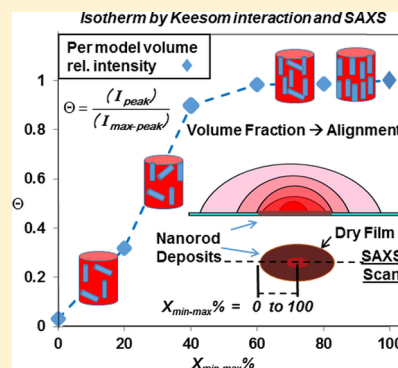
SEE PROFILE

## Evaporation Assisted CdSe Nanorod Assembly by Small Angle X-ray Scattering and Langmuir Adsorption

Kimani A. Stancil\*

Department of Physics and Astronomy, Howard University, 2355 Sixth Street NW, Washington, District of Columbia 20059, United States

**ABSTRACT:** Using evaporative assembly of dilute (<3 wt %) CdSe nanorod solutions, we combine Langmuir adsorption and small-angle X-ray scattering (SAXS) to estimate the onset of nanorod alignment instigated by the dipolar character of CdSe nanorods. SAXS demonstrates that the peak scattering intensity increases along the diameter toward the center of each dry assembly. By agreement of SAXS and profilometry results, we have established a practical access window into the lyotropic feature of emergent orientational order or alignment in nanorod solutions. With a mean field approach involving the rod–rod or dipole–dipole interaction, i.e., Keesom interaction, and the observation that the nanorod dipole moment scales with nanorod volume, we demonstrate that reaction constants result in nanometer scale interparticle separations which increase with aspect ratio or excluded volume. We compute a SAXS weighted intensity alignment parameter, which improves with aspect ratio, to indicate edge-to-center orientational ordering within dry nanorod assemblies.



## ■ INTRODUCTION

Engineering materials to enhance optical and electronic properties is a constant thrust in photonics, plasmonics, and reconfigurable optical metamaterials.<sup>1–7</sup> By controlling dielectric contrast or the spatial variation of refraction index, the optical or photonic behavior can be tuned. Tunable photonic crystals use temperature to change the liquid crystal phase and refraction index.<sup>1,3</sup> Lyotropic or concentration sensitive material assemblies do not lend toward easy tuning because of kinetic constraints in achieving the desired phase. Consequently, emergent phases as in the case of high weight percent cadmium selenide (CdSe) nanorod solutions occur over days to weeks.<sup>8,9</sup> And, the ability to sustain order over large areas is clearly easier when using smectic nanorod assemblies<sup>10,11</sup> where there exists high monodispersity resulting in significant positional and orientational order.

Equipped with Onsager's result<sup>12</sup> that the volume fraction,  $\phi_{I-N}$  at isotropic–nematic (I–N) phase coexistence scales inversely with aspect ratio,  $L/D$ , i.e.  $\phi_{I-N} = 4/(L/D)$ , several efforts to assemble nanorods by evaporating solvent, preparing high weight percent solutions, and by adding electric fields have been explored.<sup>8–11,13–15</sup> Without a clear identification of the I–N phase coexistence using nanorods, a practical access window for tuning lyotropic features of aligned nanorods over large areas may prove elusive. Perhaps, for practical reasons, the clear discussion of kinetic influences is largely absent in attempts to establish a CdSe nanorod phase diagram.<sup>9</sup>

In this work, we estimate the onset of nanorod alignment instigated by the dipolar character of CdSe nanorods. Notably, our efforts combine small-angle X-ray scattering (SAXS), profilometry, and Langmuir adsorption<sup>16,17</sup> to analyze dry nanorod deposits with different aspect ratio. Dilute (<3 wt %) CdSe nanorod-methylcyclohexane solutions evaporate as

shown in Figure 1A to form circular dry assemblies. During evaporation, we observe material deposits that precipitate from

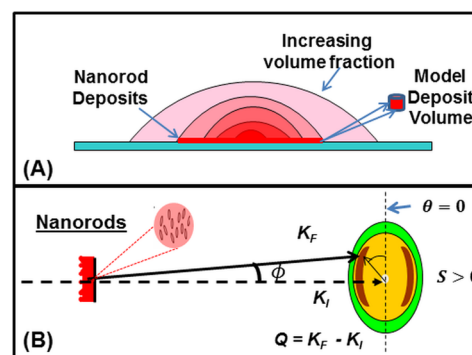


**Figure 1.** (A) CdSe nanorod–methylcyclohexane assembly—nanorod deposits precipitate as the solution–substrate–vapor contact line recedes. Nanorods occupy a model deposit volume before precipitating. (B) Small angle X-ray scattering of CdSe nanorods on a substrate—the scattering vector,  $\mathbf{Q} = \mathbf{K}_F - \mathbf{K}_I$ , (measured by the 2-D detector) shows planar vertical orientations with positive intensity weighted alignment values ( $S > 0$ , defined in eq 1).

a small volume at the drop's periphery where the substrate–solution–vapor contact line uniformly recedes. In addition, we observe a pink to red transition in solution color that indicates an increase in bulk solute concentration. We define the small volume at the drop's periphery as the model deposit volume from

Received: August 24, 2014

Revised: November 16, 2014

Published: November 20, 2014



which we visualize the drying process and the application of the Langmuir adsorption model to our small-angle X-ray scattering (SAXS) results. Small angle X-ray scattering in Figure 1B measures the scattering vector,  $Q$ , equal to the difference between the final ( $K_F$ ) and initial ( $K_I$ ) propagation vectors, i.e.  $Q = K_F - K_I$ . With SAXS, we determine the inter-rod spacing, and the orientational order with an intensity weighted alignment factor,  $S$ . For  $S > 0$ , nanorods are vertically parallel to the substrate as shown in Figure 1B, and for  $S < 0$ , nanorods tend to lie horizontal in the substrate plane. The technical explanation of alignment begins with eq 1 in the next section.

Typical coffee staining models consider solute precipitation to be a random fluid driven process, and pinning of the contact line tends to result in most solute occupying a dense outer ring.<sup>18–20</sup> The solute deposits can be considered as a combination of random and ordered solute. And generally, we assume that CdSe nanorods experience attractive interactions resulting from the anisotropic polarizability and nanorod dipole moment.<sup>21</sup> van der Waals, and other short or long-range forces are present, however, we focus our considerations on the Keesom interaction<sup>22</sup> to show that the dipole–dipole interaction likely prevails in forming our nanorod assemblies. Initially, by choosing to study quartz (hydrophilic) and SU8 (hydrophobic) substrates, we aimed to examine the potential for using hydrophilic/hydrophobic cross patterning toward sub-60 nm nanocrystal confinement similar to previous studies including tetrapods.<sup>23,24</sup> Post-study, we believe that the substrates differentiate wetting conditions, but as a secondary influence to the average dipole–dipole interaction's influence on nanorod assembly. To present our results, we focus on quartz substrates for 4 nanorod batches with different aspect ratio.

During evaporation, competing solvent and nanoparticle phase transitions progress under nonequilibrium conditions with changes on large length scales due to interparticle interactions.<sup>25</sup> A completed evaporation experiment produces a range of potentially accessible volume fractions that depend on the initial solution preparation, and the rate or control of the evaporation conditions. In principle, the CdSe solution's refraction index can be tuned by selecting the nanoparticle's volume fraction as has been shown with gold (Au) nanoparticles in *n*-dodecane.<sup>26</sup> With our work, the model deposit volume at the drop periphery is in open contact with the bulk volume, and serves as a sample of the concentrating nanorod mixture. On the basis of precipitation in the resulting dry assembly, we consider the model deposit volume to be no smaller than the SAXS scattering volume established by the X-ray beam cross-section and nanorod film height. The nanorod film height is measured using profilometry. In Figure 1A, nanosolute is driven into the model volume by a dynamic combination of fluid flows, and surface forces. Interparticle interactions increase as more nanosolute occupies the same model volume. And in the case of dipole–dipole interactions, the interparticle forces are tunable by size and shape since the CdSe dipole moment,  $u_z$ , scales linearly with the nanoparticle or nanorod volume, i.e.  $u_z = (0.19 \text{ } \mu\text{C}/\text{cm}^2)(V_{\text{nanorod}})$ .<sup>21</sup> Another specific contribution of this work is that by using the Langmuir adsorption isotherm for analysis, reaction constants can be derived that depend on the particle interaction energies.

## EXPERIMENTAL METHODS

CdSe nanorods are synthesized with a combination of trioctyl phosphine oxide (TOPO), hexyl phosphonic acid (HPA), and tetradecyl phosphonic acid (TDPA) ligands using dimethyl cadmium ( $\text{CdMe}_2$ ) precursor by established recipe.<sup>27</sup> From low weight percent ( $<3 \text{ wt } \%$ ) nanorod–methylcyclohexane solutions, small volumes, (0.05 mL) are deposited on level quartz or SU8 coated quartz surfaces. Quartz wafers (HOYA 4W 55, 525  $\mu\text{m}$  thick) were selected for measure of optical birefringence and small-angle X-ray scattering on the same sample. Photolithography was used to make SU8 coatings. Note that sample solutions are stable in a closed vial at room temperature ( $\sim 20^\circ\text{C}$ ), and show good solute retention until the final drying stages.

**Sample Characterization.** All nanorod statistics were obtained using Image Pro software and a Tecnai G2 S-Twin transmission electron microscope (TEM, 200 kV). The TEM statistics in Table 1 include the average width ( $D$ ), length ( $L$ ),

**Table 1. CdSe Nanorod TEM Statistics and Prepared Solution wt %**

$D$ (nm)	$L$ (nm)	$L/D$	wt %
$3.8 \pm 0.7$	$13.2 \pm 1.6$	$3.6 \pm 0.7$	0.83
$3.7 \pm 0.6$	$23.0 \pm 5.1$	$6.3 \pm 1.5$	2.10
$4.0 \pm 0.8$	$44.8 \pm 9.4$	$11.7 \pm 3.3$	0.84
$3.7 \pm 0.7$	$45.1 \pm 11.6$	$12.4 \pm 3.5$	2.96

and aspect ratio ( $L/D$ ) for each batch of nanorods, and TEM micrographs are shown in Figure 2. Approximately,  $\sim 200\times$

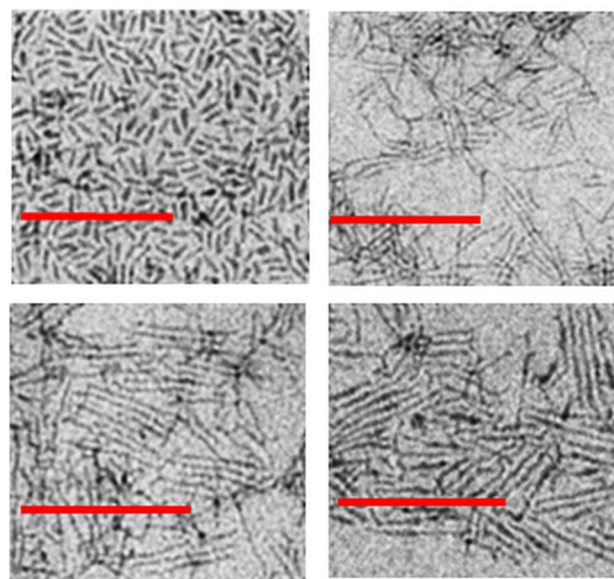


**Figure 2.** CdSe nanorod TEM micrographs.  $L/D = 3.6 \pm 0.7$  (top left);  $L/D = 6.3 \pm 1.5$  (top right);  $L/D = 11.7 \pm 3.3$  (bottom left);  $L/D = 12.4 \pm 3.5$  (bottom right). The scale bar is 100 nm in all micrographs.

nanorods were measured individually per batch. Note that the aspect ratio was determined for each rod sampled and then averaged per batch. The aspect ratio in Table 1 is the batch value per solution from which multiple samples were extracted for identical use on quartz or SU8. Optical birefringence was observed using a NIKON E600 POL microscope. And order in

each dry assembly was confirmed with small-angle X-ray scattering (SAXS) using a beam with cross-sectional area,  $A_{\text{SAXS}} = 100 \mu\text{m} \times 700 \mu\text{m}$ , at the Lawrence Berkeley Laboratory Advanced Light Source (ALS) beamline, ALS BL 7.3.3.<sup>28</sup> Using a KRUS instrument, the water contact angles measured  $\sim 25^\circ$  and  $\sim 85^\circ$  for quartz and SU8 surfaces, respectively. ASIQ profilometry was performed on all dry CdSe nanorod assemblies.

Oriental order was confirmed using SAXS as shown in Figure 1B. The substrate is perpendicular to the incident beam (wave vector,  $\mathbf{K}_i$ ), and the X-ray scatters (with a final wave vector,  $\mathbf{K}_f$ ) at an angle  $\phi$ . The scattering vector,  $\mathbf{Q} = \mathbf{K}_f - \mathbf{K}_i$  has a magnitude  $Q = 4\pi \sin(\phi/2)/\lambda$  with wavelength,  $\lambda = 0.124$  nm. 1-D plots,  $I$  (cps) vs  $Q$  ( $\text{\AA}^{-1}$ ), provide a look at both the inter-rod spacing (located at intensity peaks,  $I_{\text{peak}}$ , that correspond to nanorod width at high  $Q$ ) and structure expressed through the form and structure factors that contribute to the scattered intensity. By analysis of the 2-D Detector image, and through a combination of Igor Pro with NIKA plug-in<sup>29</sup> and Microsoft Excel, an alignment parameter was computed for points along the diameter of each assembly.

The alignment parameter,<sup>30</sup>  $S$ , in eq 1 measures nanorod orientation.

$$S = \frac{-2 \int_0^{\pi/2} I_{C,\text{avg}}(\theta) P_2(\cos(\theta)) \sin(\theta) d\theta}{\int_0^{\pi/2} I_{C,\text{avg}}(\theta) \sin(\theta) d\theta} \quad (1)$$

In the transmission geometry,  $\theta$ , is the rotation angle in the detector and substrate plane with  $\theta = 0^\circ$  along the vertical.  $P_2(\cos(\theta)) = (1/2)(3 \cos^2(\theta) - 1)$ , is the second order Legendre polynomial.  $I_{C,\text{avg}}$  is the pixel averaged intensity along the radial direction using NIKA software.<sup>29</sup> Both  $I_{C,\text{avg}}$  and  $P_2(\cos(\theta))$  uncover the mean orientational ordering. The nanorod's short axis (i.e., width) may align with  $\theta = 90^\circ$  and  $270^\circ$ , requiring that the long axis (i.e., length) be vertical with positive values ( $S > 0$ ) as shown in Figure 1B.

A 0.05 mL volume of CdSe solution is deposited. Once drying is complete, each SAXS line scan with point collections of 120 s separated by 0.5 mm over  $2d$ , where  $d$  is the diameter of each assembly in mm ensures that the ( $\approx 2$ –5 mm sized) diameter is fully sampled.

## RESULTS AND DISCUSSION

We clarify a useful correlation between SAXS and the Langmuir adsorption, by examining the X-ray scattering intensity dependence on volume fraction. And we consider the adsorption covering ratio as it matches the amount of nanorods deposited along the assembly diameter as the fluid contact line recedes. Formally, SAXS and Langmuir adsorption are connected by the small-angle X-ray scattering dependence on volume fraction for N-particle assemblies with either spherical or rod shape. For rods in nematic, or aligned configurations with identical interparticle interactions, we begin with eqs 2 and 3 which express the scattering intensity's dependence on number density or concentration,  $(N/V)$ , structure factor,  $S(Q)$ , the rod volume,  $V_{\text{rod}}$  and the form factor,  $P(Q)$ .<sup>31</sup>

$$I(Q) = \left(\frac{N}{V}\right) \times S(Q) \times (V_{\text{rod}})^2 \times P(Q) \quad (2)$$

$$I(Q) = \phi \times S(Q) \times V_{\text{rod}} \times P(Q) \quad (3)$$

$\phi$  is the volume fraction that equals the number of rods,  $N$ , multiplied by the volume per rod,  $V_{\text{rod}}$ , and divided by the total scattering volume,  $V = V_{\text{scat}}$ . In eq 4,

$$\phi = \left(\frac{NV_{\text{rod}}}{V}\right) = \left(\frac{V_{\text{rods}}}{V}\right) \quad (4)$$

$V_{\text{rods}}$  is the total volume of nanorods in a volume,  $V$ . On the basis of the nanorod shape, which we model as a cylinder, the form factor,  $P(Q)$ , does not change substantially within a batch. For the structure factor, we consider the equation,  $S(Q) = 1 - v\pi s^2[2J_1(Qs)/Qs]$  by Oster and Riley, for cylinders oriented perpendicular to the incident X-ray's direction.<sup>32</sup> The structure factor can be computed with the areal number density,  $v = N/A$ , where  $A$  is the cross-sectional area occupied in the plane of incidence or the plane perpendicular to the cylinder's long axis; also with the center-to-center interparticle separation,  $s$ , and a first order Bessel function,  $J_1(Qs)$ . We assume a close-packed structure for each nanorod deposit of the same dry assembly with a center-to-center interparticle separation,  $s \sim 2\pi/Q_{\text{peak}} \approx D_{\text{peak}}$  (listed in Table 2 for different aspect ratio assemblies) and

**Table 2.**  $Q_{\text{peak}}$ ,  $D_{\text{peak}}$ , and  $z_{\text{profile}}$ : SAXS and Profilometry (on Quartz)

$L/D$	$Q_{\text{peak}}$ ( $\text{\AA}^{-1}$ )	$D_{\text{peak}}$ (nm)	$z_{\text{profile}}$ (nm)
3.6	$0.107 \pm 0.003$	$5.85 \pm 0.17$	20978.4
6.3	$0.137 \pm 0.001$	$4.57 \pm 0.04$	11310.9
11.7	$0.118 \pm 0.003$	$5.33 \pm 0.15$	14389.0
12.4	$0.122 \pm 0.003$	$5.14 \pm 0.12$	9664.8

areal number density,  $v \sim 1/D^2$ , where  $D$  is the nanorod width determined by TEM in Table 1. Therefore, we consider the structure factor to be practically the same for all nanorod deposits representing the same dry assembly and aspect ratio.

Effectively, our window into the mean nanorod assembly behavior is gained by the estimate that the relative peak intensity is proportional to the relative volume fraction of the model deposit volume, i.e.  $(I_{\text{peak}}/I_{\text{max-peak}}) \sim (\phi_{\text{dep}}/\phi_{\text{max}})$ . Subscripts "dep" and "max" refer to the nanorods deposited and their maximum number deposited from the model deposit volume.

The volume per rod,  $V_{\text{rod}} = \pi LD^2/4$ , is determined by the length,  $L$ , and diameter,  $D$ , measured by TEM. The scattering volume,  $V_{\text{scat}}$ , is equal to the X-ray beam size multiplied by an assembly's average height,  $z$  (nm) =  $z_{\text{profile}}$  determined by profiling (and listed in Table 2), i.e.,  $V_{\text{scat}} = A_{\text{SAXS}} z_{\text{profile}}$ . For SAXS, the total volume,  $V$ , equals the scattering volume which in effect is equal to the minimum model deposit volume depicted in Figure 1A. The bulk solution volume fraction is also proportional to the concentration,  $C_{\text{sol}}$  i.e.,  $\phi_{\text{sol}} = C_{\text{sol}} V_{\text{rod}}$ .

A quick review of our experiment demonstrates that during evaporation, we observe a volume decrease as nanorods precipitate at the receding substrate-solution-vapor contact line. Physically, in Langmuir adsorption, increases in equilibrium pressure or concentration result in an increase in surface coverage to unity or to a saturation limit. Equivalently, we observe by evaporation that increases in concentration or bulk volume fraction increase the number of nanorods deposited at the receding drop's periphery until drying is complete. Therefore, the Langmuir covering ratio,  $\Theta$ , in eq 5, can be linked to SAXS using the volume fraction.



$$\Theta = \frac{N_{dep}}{N_{max}} = \frac{k_r C_{sol}}{(1 + k_r C_{sol})} = \frac{k_r \phi_{sol}/V_{rod}}{(1 + k_r \phi_{sol}/V_{rod})} = \frac{\phi_{dep}}{\phi_{max}} \quad (5)$$

The Langmuir covering ratio expresses the surface coverage for a set solution concentration,  $C_{sol}$  with reaction constant,  $k_r$ . And it describes the nanorods deposited,  $N_{dep}$ , relative to the maximum,  $N_{max}$ , deposited in the final drying step. This ratio is also equal to the relative volume fraction, i. e.  $\phi_{dep}/\phi_{max}$  or equivalently, the ratio of volume fractions that reference the same model deposit volume. The determined reaction constant,  $k_r \sim \exp(E/(k_B T))$  enables energy estimates based on nanorod assembly, and an experimental connection between Langmuir adsorption and SAXS of N-particle assemblies is proven by our results.

In Figure 3A, a sample,  $I$  (cps) vs  $Q$  ( $\text{\AA}^{-1}$ ) plot for  $L/D = 6.3 \pm 1.5$  is shown for diameter scans in 0.5 mm increments where

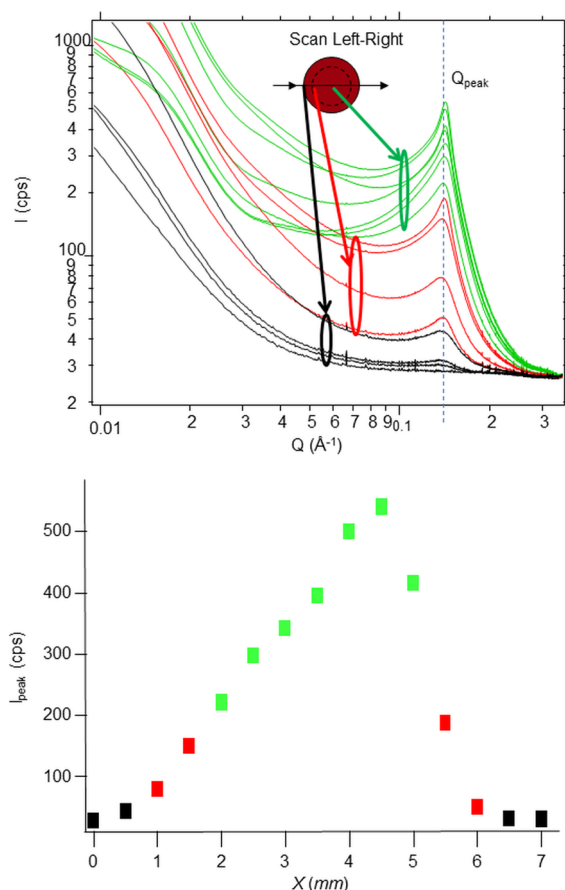


**Figure 3.** (A) Sample SAXS plot,  $I$  (cps) vs  $Q$  ( $\text{\AA}^{-1}$ ) for  $D = 3.7 \pm 0.6$  nm,  $L = 23.0 \pm 5.1$  nm,  $L/D = 6.3 \pm 1.5$ , with initial wt % = 2.10.  $Q_{peak} = 0.1392 \pm 0.0026 \text{ \AA}^{-1}$  and  $D_{peak} = 4.5 \pm 0.08$  nm. Curves span edge (black), intermediate (red), and central (green) regions of each assembly. (B) Peak intensity,  $I_{peak}$  (cps) vs  $X$  (mm), the scan position, with assembly diameter = 4.5 mm, which spans the edge, middle, and central regions.

the scattering peaks (for the same aspect ratio batch),  $I_{peak}$  (cps) vs position,  $X$  (mm) are analyzed in Figure 3B. In parts A and B of Figure 3, scattering from the edge (black curves), middle (red curves), and central (green curves) regions is shown. The scattering increases toward the center of each assembly at a scattering vector  $Q_{peak}$  or with characteristic spacing,  $D_{peak}$  in

Table 2 that closely matches the nanorod (plus ligand) size by TEM in Table 1. The increasing trend in peak intensity,  $I_{peak}$ , through application of eq 5 and the following eqs 6, 7, and 8 substantiate the Langmuir adsorption-SAXS connection in this study. In Table 2 (on quartz), we list the mean peak scattering vector,  $Q_{peak}$ , and interparticle spacing,  $D_{peak}$ , for each nanorod batch. Also included in Table 2 is the film thickness,  $z_{profile}$ .

In eq 6, the relative peak scattering intensity,  $(I_{peak}/I_{max-peak})$  enables the covering ratio in eq 5 to be rewritten to include the bulk solution volume,  $V_{sol}$  and the fit constant,  $a$ , is shown by eq 7 to be proportional to the reaction constant,  $k_r$ . We use a spherical cap to model the solution volume as  $V_{sol} = V_{s-cap}(r, \theta_{mc}) = f(\theta_{mc})r^3$  with  $\theta_{mc}$  equal to the methylcyclohexane contact angle estimated by the water contact angle,  $\theta_{H_2O}$ , i.e.  $\theta_{mc} = 90^\circ - \theta_{H_2O}$ .

$$\frac{\phi_{dep}}{\phi_{max}} \cong \frac{(I_{peak})}{(I_{max-peak})} = \frac{(a/V_{sol})}{(1 + a/V_{sol})} \quad (6)$$

$$k_r = \left( \frac{\pi L D^2}{4} \right) \left( \frac{a}{V_{sol} * \phi_{sol}} \right) \quad (7)$$

With our nanorod recipes, we assume that nanorods precipitate with comparable solubility limits. The fluid contact line recedes and a percentage distance along the diameter based on profilometry is used to unite nanorod drying behavior for different aspect ratios. Each dry deposit position matches a distance value,  $d_{scale}$  (mm), used to calculate a drop radius,  $r = r_{sol}$  (i.e.,  $d_{scale} = 0$  at the outer edge of each assembly). We introduce  $d_{max-peak}$ , the distance from the edge to the  $d_{scale}$  position value of the maximum peak scattering intensity,  $I_{max-peak}$ . We define a radius,  $r_{scat}$ , for matching the minimum spherical cap volume,  $V_{s-cap}$ , to the scattering volume,  $V_{scat}$ . For  $r_{sol}$  we add  $2r_{scat}$  to the difference,  $(d_{max-peak} - d_{scale})$  to ensure (at the maximum peak position) an effective nonzero reference bulk drop volume,  $V_{sol} = 8V_{scat}$  at  $d_{scale} = d_{max-peak}$  with  $r_{scat} = (V_{scat}/f(\theta_{mc}))^{1/3}$ .

The Langmuir data analysis begins with  $(I_{peak}/I_{max-peak})$  vs  $(1/V_{sol})$  plots where from a reciprocal fit, i.e., eq 8, in Figure 4, both the maximum intensity,  $I_{max-peak}$  can be checked and the fit constant,  $a$ , is determined.

$$\frac{(1/V_{sol})}{(I_{peak})} = \frac{(1/V_{sol})}{(I_{max-peak})} + \left( \frac{1}{(I_{max-peak}) \times a} \right) \quad (8)$$

In Figure 4(top), the full model fits (with  $V_{sol} = 8V_{scat}$ ) show good ( $R^2 > 0.98$ ) linear behavior except for the smallest aspect ratio nanorods on a SU8 substrate. In Figure 4(bottom), modified fits (without  $V_{sol} = 8V_{scat}$  and the poor fit for lowest aspect ratio on SU8 substrate removed) show good ( $R^2 > 0.98$ ) linear behavior except for the smallest aspect ratio nanorods on quartz. Other than the SAXS measurement, there is no strongly apparent difference (including optical birefringence) in assemblies on quartz and SU8 for  $L/D = 3.6 \pm 0.7$ , the smallest aspect ratio batch. We presuppose an increase in translational entropy on SU8 due to better wetting by methylcyclohexane, but this is beyond the experimental scope of our present work.

Initially, all batches are considered sufficiently dilute that an ordered phase is not observed, but during evaporation and by ignoring the inter-nanorod dipole-dipole interaction, the increase in volume fraction should progress toward I-N

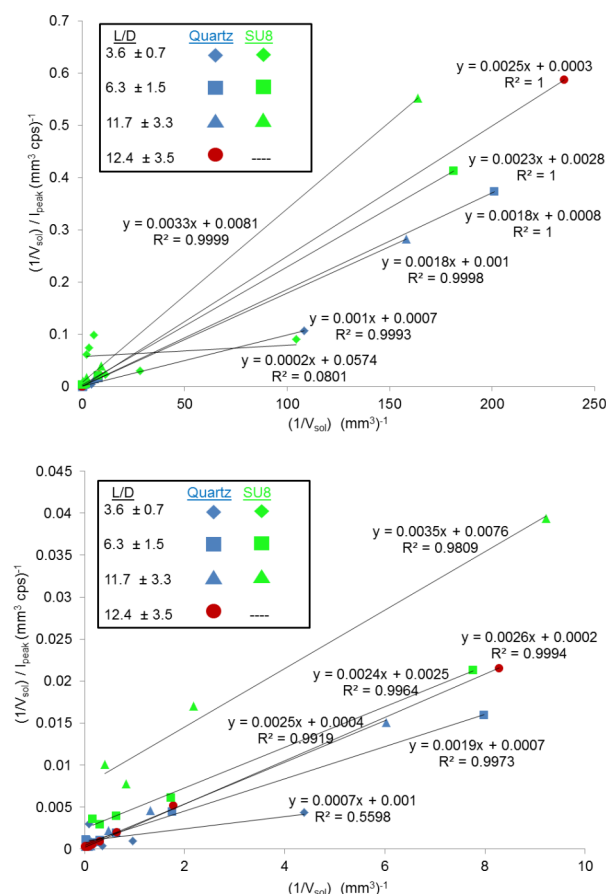


**Figure 4.** Langmuir reciprocal plots  $[(1/V_{\text{sol}})/I_{\text{peak}}] = [(1/V_{\text{sol}})/I_{\text{max-peak}}] + [1/(I_{\text{max-peak}} \times a)]$  for fitting  $a$  and  $I_{\text{max-peak}}$ . (Top) Full fit using a nonzero reference bulk volume (at the maximum peak position),  $V_{\text{sol}} = 8V_{\text{scat}}$  with one bad fit shown for lowest aspect ratio on SU8. (Bottom) Modified fit without reference bulk volume, with smallest aspect ratio on SU8 not shown due to negative slope fit. All fits shown exhibit  $R^2 > 0.98$  except the smallest aspect ratio ( $L/D = 3.6 \pm 0.7$ ) on SU8 (full/modified fit) and quartz (modified fit).

phase coexistence. By including the CdSe nanorods' attractive dipole–dipole interactions, we expect nanorod alignment to emerge. We examine this view in Figure 5 by computing an intensity weighted order parameter or (dimensionless) alignment factor (from eq 1),  $S$ , vs the (dimensionless) relative position along the assembly,  $X\%$ , for dry assemblies on quartz (solid curves) and SU8 (dashed curves). Only 3 nanorod batches were compared since the batch with largest aspect ratio ( $L/D = 12.4 \pm 3.5$ ) partially delaminated from SU8 prior to SAXS measure. Each curve in Figure 5 displays the incidence of alignment along an assembly's diameter. There is a higher incidence of alignment for large aspect ratio nanorods, and we note that ( $L/D = 11.7 \pm 3.3$ ) solutions align earlier at the assembly edges. All quartz results maintain clear incidence of alignment in a range,  $X\% = 35\text{--}75\%$  spanning intermediate and central regions an assembly. Considering the increases in  $I_{\text{peak}}$  toward the center of an assembly, there is a progressive increase in alignment with increasing concentration,  $C_{\text{sol}}$ , or bulk volume fraction,  $\phi_{\text{sol}}$ . As an example, one can compare the red-solid curve in Figure 5 with Figure 3b  $I_{\text{peak}}(\text{cps})$  vs  $X(\text{mm})$  plot for the same aspect ratio solution ( $L/D = 6.3 \pm 1.5$ ). Alignment results on SU8 are similar but not as pronounced. For example, lowest aspect ratio ( $L/D = 3.6 \pm 0.7$ ) batch on SU8 did not exhibit any significant orientational order. Note that  $S > 0$  along

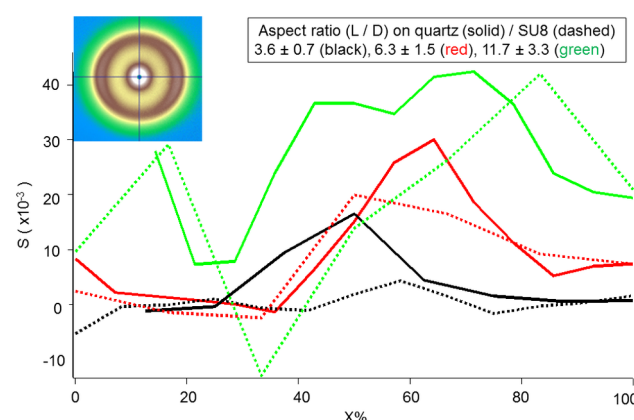


**Figure 5.** Orientational order in nanorod deposit.  $S$  vs  $X\%$ : alignment vs relative position along diameter scan. Aspect ratios: ( $L/D = 3.6 \pm 0.7$  (black curves),  $L/D = 6.3 \pm 1.5$  (red curves), and  $L/D = 11.7 \pm 3.3$  (green curves) are shown for quartz (solid) and SU8 (dashed) substrates. The 2-D detector image (top-left) and  $S > 0$  show that nanorods align perpendicular to the diameter. Note that  $S$  and  $X\%$  are dimensionless relative quantities.

a diameter scan also suggests that nanorods lie parallel to the receding fluid contact line which is expected when nanorods align at an interface to minimize their interfacial free energy.<sup>33</sup>

With the Langmuir fits, we establish the reaction constant,  $k_r$ , and for the peak intensities, we calculate the volume fraction,  $\phi_{\text{sol}}$ . The volume fraction depends on the covering ratio,  $\Theta$ , the reaction constant,  $k_r$ , and nanorod volume,  $V_{\text{rod}}$ , i.e.  $\phi_{\text{sol}} = [\Theta/(1-\Theta)] * [V_{\text{rod}}/k_r]$ . Note that the reaction constant,  $k_r$ , is estimated by three parameters: (1) the fit constant,  $a$ ; (2) the volume of each rod,  $V_{\text{rod}}$  determined by TEM ( $D$ , and  $L$ ); and (3) the initial weight percent listed in Table 1, which by careful consideration of the component densities ( $\rho_{\text{methylcyclohexane}} = 0.77 \text{ g/cm}^3$ ;  $\rho_{\text{CdSe}} = 5.81 \text{ g/cm}^3$ ) enables the calculation of the initial volume fraction,  $\phi_{\text{sol}}$ , whereby evaporation is slow enough such that  $\delta(V_{\text{sol}} \phi_{\text{sol}}) = \delta N \approx 0$ .

To estimate I–N phase coexistence or the onset of nanorod alignment due to evaporation, we compare different aspect ratio batches using the correspondence between the volume fraction,  $\phi_{\text{sol}}$ , and the relative position or occurrence of a nanorod deposit. For insight, we consider our earlier discussion with the Langmuir model by plotting for all batches, in Figure 6, the dimensionless covering ratio,  $\Theta$  vs the relative position (also dimensionless),  $X_{\text{min-max}}\%$ , corresponding to the edge-to-center peak intensities (as shown for  $L/D = 6.3 \pm 1.5$  in Figure 3, parts A and B). Note that  $X_{\text{min-max}}\% \neq X\%$  (used in Figure 5). And we note, in the lower right inset for Figure 6, that the best profilometry–SAXS correspondence plot observed (by eye using an arbitrary constant of proportionality) occurs on quartz at high aspect ratio,  $L/D = 12.4 \pm 3.5$ . This is a clear visual impression of Langmuir isotherm saturation behavior, where the thin film height scales with the amount of nanorods deposited. Using profilometry for the height (nm) vs diameter ( $\mu\text{m}$ ) of each assembly with  $0.4 \mu\text{m}$  in width and  $0.0012 \text{ nm}$  ( $0.012 \text{ \AA}$ ) thickness resolution, we average the profilometry data over  $0.5 \text{ mm}$  intervals to match SAXS data. On the basis of our fitting procedure, we compare all batches using the same relative position scaling in Figure 6, and match the Langmuir isotherm determined volume fractions to the relative positions of the edge-to-center peak scattering intensities,  $\phi$  vs  $X_{\text{min-max}}\%$ . We then establish a series of exponential curve

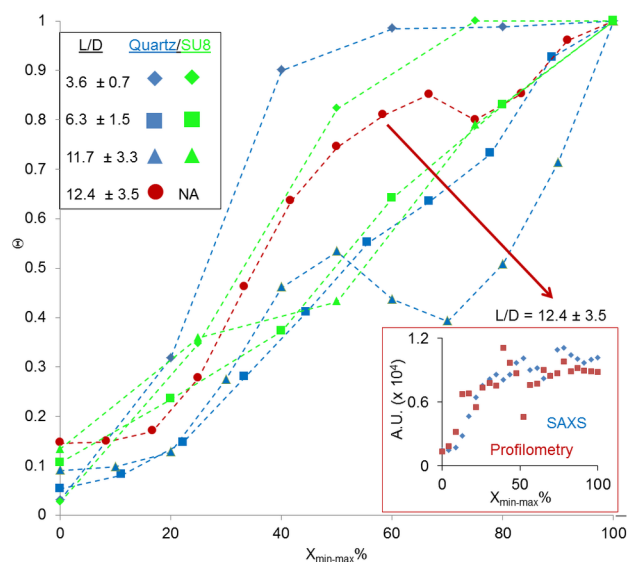


**Figure 6.** Covering ratio,  $\Theta$ , vs  $X_{\min-\max}$  %, relative distance from edge-to-center or from the minimum to maximum peak scattering intensity. All tested aspect ratios are shown. SAXS–profilometry correspondence for  $L/D = 12.4 \pm 3.5$  (red) is given in the lower right inset which gives a physical impression of the characteristic Langmuir adsorption isotherm. Note  $\Theta$  and  $X_{\min-\max}$  % are dimensionless.

fitted volume fraction (i.e.,  $\phi = \phi_{\text{sol-fit}}$ ) equations for each aspect ratio.

At relative positions from  $X_{\min-\max}$  % = 0% to 100% in 5% intervals, we compare volume fractions using the log equation form for Onsager's estimate of I–N phase coexistence,  $\log \phi = -m \log(L/D) + b$  where  $m = 1$  and  $b = \log 4$ . In general,  $\exp(b) = c^*$  is the bifurcation point between isotropic and nematic phases<sup>34</sup> but this is somewhat ill-defined with attractive interactions present. The best-fit on quartz occurs at a position  $X_{\min-\max}$  % = 35% where slope and intercept match  $m = 1.4233$  and  $b = -0.7188$  respectively ( $R^2 = 0.8223$ ). For SU8 at the same position, the slope and intercepts are  $m = 1.1564$  and  $b = 0.0845$  ( $R^2 = 0.8328$ ). However, at position,  $X_{\min-\max}$  % = 30%, both SU8 and quartz exhibit almost identical slopes,  $m_{\text{quartz}} = 1.2462$ , and  $m_{\text{SU8}} = 1.2239$ , with intercepts  $b_{\text{quartz}} = -0.9872$  and  $b_{\text{SU8}} = 0.0016$  (with  $R^2 = 0.8073$ ;  $R^2 = 0.8154$ ). The slopes are near the expected value of  $m = 1$ , and the intercepts are different, but as is apparent and consistent with our system, we cannot obtain the bifurcation point,  $b = \log 4 = 1.3863$  or  $c^* = 4$ , for volume fraction  $\phi = c^*/(L/D)$ . Empirically, the log–log probe successfully estimates the inverse relationship between volume fraction and aspect ratio.

For all the data, monotonic changes in the slope,  $m$ , are observed which is consistent with the preferential evaporation driven changes in volume fraction. In the remaining discussion, the positions  $X_{\min-\max}$  % = 30% or 35%, define the points of “I–N onset” or points at which rods align during evaporation. The determination of the I–N onset points tracks well with our computed intensity weighted order parameter,  $S$  vs  $X$  % in Figure 5. And by comparing the I–N onset point to the emergence of order in the diameter scan, we find that the point,  $X_{\min-\max}$  % = 35% translates to approximately  $X$  % = 25% (from the left in Figure 5) along the diameter, thus showing good agreement with the progressive increase of the order parameter values,  $S$ , in Figure 5. However, the noncorrelated determination of the bifurcation,  $c^*$ , emphasizes that our experiment does not explore I–N phase coexistence in the ideal Onsager

context for dilute solutions.<sup>12</sup> Alternatively, we conclude that during evaporation, volume changes drive the system toward characteristic I–N behavior, whereupon nanorods interact strongly enough to influence the emergence of alignment in the resulting nanorod deposits.

Effectively, nanorods and solvent molecules transition from liquid to condensed phase and vapor, respectively. We observe that this process should be reversible since in a related study, we can recover nanorod solutions by solvent addition which also leads to solvent annealing effects in microchannels.<sup>35</sup> When particle solutions wet surfaces, van der Waals forces resulting from surface, particle, and dispersion influences determine particle assembly.<sup>36</sup> In the context of the SAXS-constructed Langmuir model in this work, nanorod–nanorod interactions are significant when a non-negligible nanorod occupation of the model deposit volume occurs.

van der Waals interactions may apply when the separation distance,  $d$ , is much less than the nanorod radius, however all SAXS inter-rod spacings are near equal or greater than the TEM determined diameter. Dipole–dipole coupling has a long-range influence on the order of  $\sim 50$  nm<sup>35</sup> and considering the permanent dipole moment intrinsic to CdSe nanorods, this is the predominant coupling in the solution when transitioning to the dry assembly. We check this by noting that  $[(1 - \phi)/\phi] = V_{\text{upr}}/V_{\text{rod}}$  where  $V_{\text{upr}}$  is the unoccupied volume per rod, and estimate the weight percent (using  $V_{\text{rod}}$  based on TEM in Table 1) that would correspond to 50 nm (dipole–dipole influence) and 2 nm (i.e., nominal van der Waals influence between rods). By matching the diameter of the sphere representing  $V_{\text{upr}}$  to equal 50 and 2 nm, we calculate (using  $\rho_{\text{methylcyclohexane}} = 0.77$  g/cm<sup>3</sup>;  $\rho_{\text{CdSe}} = 5.81$  g/cm<sup>3</sup>) the weight percent, i.e., wt % =  $[1 + (((1 - \phi)/\phi)^* (\rho_{\text{methylcyclohexane}}/\rho_{\text{CdSe}}))]^{-1} \times 100\%$ . The calculated wt % for 50 nm separations or dipole–dipole influence equals 1.70 wt % ( $L/D = 3.6 \pm 0.7$ ), 2.77 wt % ( $L/D = 6.3 \pm 1.5$ ), 6.09 wt % ( $L/D = 11.7 \pm 3.3$ ), and 5.29 wt % ( $L/D = 12.4 \pm 3.5$ ). All calculated wt % are greater than the initially prepared wt % from Table 1 suggesting that evaporation enables solutions to concentrate enough for dipole–dipole interactions to be significant. Alternatively, to approach separations where the van der Waals influence is relevant, all solutions must evolve toward  $\sim 99$  wt % which may be unobservable due to evaporation rates and precipitation in the final drying stage. In effect, assembly in solution appears to be primarily influenced by the dipole–dipole interaction. Therefore, we focus on the surface and dipole–dipole interaction (or thermally averaged Keesom interaction).

We adopt a mean-field perspective where instead of the traditional Langmuir model of a nanorod being attracted by a surface with energy cost,  $E_{\text{surface}} > 0$ , we recognize the attraction by other nanorods within solution with energy,  $E_{\text{rod-rod}} < 0$  prior to precipitation. By application of the Keesom interaction between dipoles, we consider the energy associated with nanorod deposition as a description of dominant rod–rod vs actual surface interactions while the rods still remain in solution, i.e.,  $E = E_{\text{surface}} + E_{\text{rod-rod}} \approx E_{\text{rod-rod}}$ . The subsequent precipitation likely arises due to solubility limits reached at diminishing volumes near the receding contact line. The reaction constant is a rate limiting parameter highlighting the energy barrier associated with nanorod aggregation and precipitation with preferential dipolar alignment. In eq 9, the mean-field energy,  $E_{\text{rod-rod}}$  is set equal to the thermally averaged Keesom interaction energy between nanorods with dipole moments,  $u_i$ , for  $i = 1, 2$ . The interparticle separation,  $r_k$



is highlighted with respect to the permittivity of free space,  $\epsilon_0$ , the Boltzmann constant,  $k_B$ , and the absolute temperature,  $T$ .

$$\frac{E_{\text{rod-rod}}}{k_B T} = \frac{-u_1^2 u_2^2}{(4\pi\epsilon_0)^2 (k_B T)^2} \frac{2}{3} \frac{1}{r_k^6} \quad (9)$$

In Table 3, we use the reaction constants to match the energy,  $E = E_{\text{rod-rod}}$ , equal to the Keesom energy. Then, by

**Table 3. Langmuir Constants, ( $a$ ,  $k_r$ ), Relative Energy Cost,  $E/k_B T$ , and Keesom Interparticle Separation,  $r_k$  (on Quartz)**

$L/D$	$a$	$k_r$	$E/k_B T$	$r_k$ (nm)
3.6	1.4	3.83e-15	-14.4173	3.6
6.3	2.3	3.95e-15	-14.4037	5.0
11.7	1.8	1.78e-14	-13.7491	8.7
12.4	8.3	1.01e-14	-13.9945	8.0

applying the result from Liang–Shi Li et al. that  $u_z = (0.19 \mu\text{C}/\text{cm}^2)$  ( $V_{\text{nanorod}}$ ) or that the nanorod dipole moment scales with nanorod volume (i.e.,  $V_{\text{nanorod}} = V_{\text{rod}}$ ),<sup>21</sup> we calculate the interparticle or nanorod–nanorod separation,  $r_k$ , listed in Table 3.

The particle separation is found to be on the order of nanometers (nm) and not equal to the SAXS determined  $D_{\text{peak}}$  values (in Table 2) which may distinguish the surface vs solution impact on assembly. And by plotting the separation,  $r_k$ , vs aspect ratio,  $L/D$ , in Figure 7, excellent linear fits highlight a

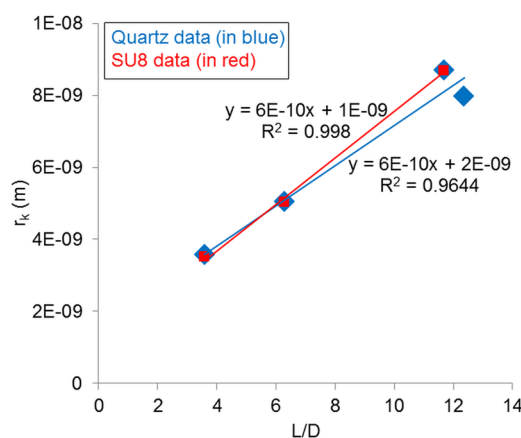


**Figure 7.** Keesom inter-rod separation,  $r_k$  (m), vs aspect ratio,  $L/D$ . Keesom dipole–dipole separation,  $r_k$ , using  $u_z = (0.19 \mu\text{C}/\text{cm}^2)$  ( $V_{\text{nanorod}}$ ). Nanorod behavior on quartz (blue) and SU8 (red) substrates show dependence on aspect ratio, i.e., excluded volume. Note that  $L/D$  is dimensionless.

strong dependence on nanorod shape and size through aspect ratio. Underlying this result is the consideration that the nanorods concentrate enough to approach excluded volume limits where the dipole–dipole or nanorod–nanorod interaction is strongest. In Figure 7, note that if we remove the higher aspect ratio batch,  $L/D = 12.4 \pm 3.5$ , the result on quartz and SU8 becomes identical by fit. Using our mean-field estimate, we conclude that there is little difference in substrate influence exerted by quartz and SU8 substrates. Our view agrees with the observation of equivalently compact CdSe nanorod assemblies forming on aluminum foil, stainless steel, and borosilicate substrates. Robustly, our observation also extends to solutions prepared for TEM with estimated dilution as low as  $3.2 \times 10^{-4}$

wt %. We are reminded that Onsager’s I–N phase coexistence prediction does not include attractive or van der Waals interactions so for sufficiently dilute solutions, attractive interactions are neglected. And we summarize our experiment as an observation of a dual identity phase behavior. In the bulk, Onsager’s estimates may apply but in the smaller model volume near the contact line, a transition from the bulk to the condensed nanorod phase occurs where attractive interactions are significant and Onsager’s estimate does not apply. Through the open contact between the bulk and model volumes, both Onsager’s I–N phase coexistence and the aligning role of attractive influences are conjoined by this evaporation study.

## CONCLUSION

Continued efforts to tune the refraction index do involve nanorod type and interaction specific tailoring that includes surface ligands not emphasized in this study. In a more fundamental vein, we show in this work that the deposition and organization of nanorods can be controlled not just by optimum evaporation conditions, but also by the intrinsic or predominate features of the solute. This point alone is not new, but by using SAXS on dry assemblies we successfully apply the Langmuir adsorption isotherm to estimate I–N onset or the emerging nanorod alignment, based on the nanorod’s dipolar character. By using SAXS and evaporation, we have produced a window, using an adsorption model, into lyotropic aspects of changing phase or alignment behavior. Diminishing bulk volume change increases the CdSe nanorod solution concentration enough for dipole–dipole influences to set in. So, effectively, the Keesom interaction underlies a mean field picture which describes nanorod interactions that are strongest at the solution edge as expected since evaporation occurs first at the edge or at the surface layer of the drop volume. Broadly, this mean field approach should be applicable to other nanoparticle-solutions or systems where certain interparticle interactions predominantly influence the resulting assembly. The nanorod organization and control on nanoscale dimensions is encouraging and consistent with continuing efforts in nanoparticle assembly.

## AUTHOR INFORMATION

### Corresponding Author

\* (K.A.S.) E-mail: [kstancil@howard.edu](mailto:kstancil@howard.edu) or [gmkimanis@gmail.com](mailto:gmkimanis@gmail.com). Telephone: (202) 806-7665.

### Notes

The authors declare no competing financial interest.

## ACKNOWLEDGMENTS

Synthesis, TEM, assembly, and microfabrication (at the UC Berkeley Microfabrication Laboratory) was supported by the Physical Chemistry of Semiconductor Nanocrystals, KC3105, Director, Office of Science, Office of Basic Energy Sciences, of the U.S. Department of Energy (DOE) under Contract DEAC02-05CH11231. K.A.S. acknowledges A.P. Alivisatos for research support with the Lawrence Postdoctoral Fellowship Program and the Advanced Light Source beamline 7.3.3 that are supported by the same DOE contract. K.A.S. acknowledges A. Hexemer, E. Gann, and E. Schaible (ALS BL 7.3.3) for SAXS support and the Howard Nanoscale Fabrication facility and director Dr. Gary L. Harris. Partial funding for this research was provided by the Partnership for Reduced Dimensional Materials (PRDM), an NSF Partnership



for Research and Education in Materials (PREM) (Award Number DMR-1205608).

## REFERENCES

- (1) Mertens, G.; Roder, T.; Schweins, R.; Huber, K.; Kitzerow, H. S. Shift of the Photonic Band Gap in Two Photonic Crystal/Liquid Crystal Composites. *Appl. Phys. Lett.* **2002**, *80*, 1885–1887.
- (2) Erickson, D.; Rockwood, T.; Emery, T.; Scherer, A.; Psaltis, D. Nanofluidic Tuning of Photonic Crystal Circuits. *Opt. Lett.* **2006**, *31*, 59–61.
- (3) White, T. J.; Zhao, A. D.; Cazzell, S. A.; Bunning, T. J.; Kosa, T.; Sukhominova, L.; Smith, T. J.; Taheri, B. Optically Reconfigurable Color Change in Chiral Nematic Liquid Crystals Based on Indolyfulgide Chiral Dopants. *J. Mater. Chem.* **2012**, *22*, S751–S757.
- (4) Liu, Q.; Cui, Y.; Gardner, D.; Li, X.; He, S.; Smalyukh, I. I. Self-Alignment of Plasmonic Gold Nanorods in Reconfigurable Anisotropic Fluids for Tunable Bulk Metamaterial Applications. *Nano Lett.* **2010**, *10*, 1347–1353.
- (5) Golovin, A. B.; Xiang, J.; Nastishin, Y. A.; Lavrentovich, O. D. Electrically Reconfigurable Optical Metamaterials Based on Orientationally Ordered Dispersions of Metal Nano-rods in Dielectric Fluids. *Proc. SPIE 7775 Liq. Cryst. XIV* **2010**, *7775*, 777502–777504 DOI: 10.1117/12.858105.
- (6) Golovin, A. B.; Lavrentovich, O. D. Electro-Optic Effects in Colloidal Dispersion of Metal Nano-Rods in Dielectric Fluid. *Mater.* **2011**, *4*, 390–416.
- (7) Golovin, A. B.; Lavrentovich, O. D. Electrically Reconfigurable Optical Metamaterial Based on Colloidal Dispersion of Metal Nanorods in Dielectric Fluid. *Appl. Phys. Lett.* **2009**, *95*, 254104.
- (8) Li, L.-S.; Walda, J.; Manna, L.; Alivisatos, A. P. Semiconductor Nanorod Liquid Crystals. *Nano Lett.* **2002**, *2*, 557–560.
- (9) Li, L.-S.; Marjanska, M.; Park, G. H. J.; Pines, A.; Alivisatos, A. P. Isotropic-liquid Crystalline Phase Diagram of a CdSe Nanorod Solution. *J. Chem. Phys.* **2004**, *120*, 1149–1152.
- (10) Querner, C.; Fischbein, M. D.; Heiney, P. A.; Drndic, M. Millimeter-Scale Assembly of CdSe Nanorods into Smectic Superstructures by Solvent Drying Kinetics. *Adv. Mater.* **2008**, *20*, 2308–2314.
- (11) Nobile, C.; Carbone, L.; Fiore, A.; Cingolani, R.; Manna, L.; Krahne, R. Self-assembly of Highly Fluorescent Semiconductor Nanorods into Large Scale Smectic Liquid Crystal Structures by Coffee Stain Evaporation Dynamics. *J. Phys.: Condens. Matter* **2009**, *21*, 264013.
- (12) Onsager, L. The Effects of Shape on the Interaction of Colloidal Particles. *Ann. N.Y. Acad. Sci.* **1949**, *51*, 627–659.
- (13) Ryan, K. M.; Mastroianni, A.; Stancil, K. A.; Liu, H.; Alivisatos, A. P. Electric-Field-Assisted Assembly of Perpendicularly Oriented Nanorod Superlattices. *Nano Lett.* **2006**, *6*, 1479–1482.
- (14) Baker, J. L.; Widmer-Cooper, A.; Toney, M. F.; Geissler, P. L.; Alivisatos, A. P. Device-Scale Perpendicular Alignment of Colloidal Nanorods. *Nano Lett.* **2010**, *10*, 195–201.
- (15) Gupta, S.; Zhang, Q.; Emrick, T.; Russell, T. 'Self-Corralling' Nanorods under an Applied Electric Field. *Nano Lett.* **2006**, *6*, 2066–2069.
- (16) Langmuir, I. The Adsorption of Gases on Plane Surfaces of Glass, Mica and Platinum. *J. Am. Chem. Soc.* **1918**, *40*, 1361–1403.
- (17) Kubo, R.; Ichimura, H.; Usui, T.; Hashitsume, N. *Statistical Mechanics: An Advanced Course with Problems and Solutions*; North-Holland: Amsterdam, 1965.
- (18) Deegan, R. D.; Bakajin, O.; Dupont, T. F.; Huber, G.; Nagel, S. R.; Witten, T. A. Capillary Flow as the Cause of Ring Stains from Dried Liquid Drops. *Nature* **1997**, *389*, 827–829.
- (19) Deegan, R. Pattern Formation in Drying Drops. *Phys. Rev. E* **2000**, *61*, 475–485.
- (20) Deegan, R. D.; Bakajin, O.; Dupont, T. F.; Huber, G.; Nagel, S. R.; Witten, T. A. Contact Line Deposits in an Evaporating Drop. *Phys. Rev. E* **2000**, *62*, 756–765.
- (21) Li, L.-S.; Alivisatos, A. P. Origin and Scaling of the Permanent Dipole Moment in CdSe Nanorods. *Phys. Rev. Lett.* **2003**, *90*, 097402.
- (22) Atkins, P.; de Paula, J. *Atkins' Physical Chemistry*, 8th ed.; W.H. Freeman: New York, NY, 2006.
- (23) Cui, Y.; Bjork, M. T.; Liddle, J. A.; Sonnichsen, C.; Boussert, B.; Alivisatos, A. P. Integration of Colloidal Nanocrystals into Lithographically Patterned Devices. *Nano Lett.* **2004**, *4*, 1093–1098.
- (24) Liddle, J. A.; Cui, Y.; Alivisatos, A. P. Lithographically Directed Self-assembly of Nanostructures. *J. Vac. Sci. Technol. B* **2004**, *22*, 3409–3414.
- (25) Rabani, E.; Reichman, D. R.; Geissler, P. L.; Brus, L. E. Drying-mediated Self-Assembly of Nanoparticles. *Nat.* **2003**, *426*, 271–274.
- (26) Kubo, S.; Diaz, A.; Tang, Y.; Mayer, T. S.; Khoo, I. C.; Mallouk, T. E. Tunability of the Refractive Index of Gold Nanoparticle Dispersions. *Nano Lett.* **2007**, *7*, 3418–3423.
- (27) Manna, L.; Sher, E. C.; Alivisatos, A. P. Synthesis of Soluble and Processable Rod-, Arrow-, Teardrop-, and Tetrapod- Shaped CdSe Nanocrystals. *J. Am. Chem. Soc.* **2000**, *122*, 12700–12706.
- (28) Hexemer, A.; Bras, W.; Glossinger, J.; Schaible, E.; Gann, E.; Kirian, R.; MacDowell, A.; Church, M.; Rude, B.; Padmore, H. A SAXS/WAXS/GISAXS Beamline with Multilayer Monochromator. *XIV Int. Conf. Small-Angle Scattering (SAS09)* IOP Publishing J. Phys.: Conf. Ser. **2010**, *247*, 012007.
- (29) Ilavsky, J. Nika: Software for Two-dimensional Data Reduction. *J. Appl. Crystallogr.* **2012**, *45*, 324–328.
- (30) Ugaz, V. M.; Cinader, J. D. K.; Burghardt, W. R. X-ray Scattering Investigation of Highly Concentrated Poly (Benzyl Glutamate) Solutions under Shear Flow. *J. Rheol.* **1998**, *42*, 379–394.
- (31) Lindner, P.; Zemb, T. eds., *Neutrons, X-Rays and Light Scattering Methods Applied to Soft Condensed Matter*; North-Holland: Amsterdam, 2002.
- (32) Oster, G.; Riley, D. P. Scattering from Cylindrically Symmetric Systems. *Acta Crystallogr.* **1952**, *5*, 272–276.
- (33) He, J.; Zhang, Q.; Gupta, S.; Emrick, T.; Russell, T. P.; Thiagarajan, P. Drying Droplets: A Window into the Behavior of Nanorods at Interfaces. *Small* **2007**, *3*, 1214–1217.
- (34) Vroege, G. J.; Lekkerkerker, H. N. W. Phase Transitions in Lyotropic Colloidal and Polymer Liquid Crystals. *Rep. Prog. Phys.* **1992**, *55*, 1241–1309.
- (35) Stancil, K. A. Evaporation Assisted Cdse Nanorod Alignment in Micro Channels. *Int. J. Eng. Res. Technol* **2014**, *3*, 1977–1984 <http://www.ijert.org/view.php?id=8298&title=evaporation-assisted-cdse-nanorod-alignment-in-micro-channels>.
- (36) Titov, A. V.; Kral, P. Modeling the Self-Assembly of Colloidal Nanorod Superlattices. *Nano Lett.* **2008**, *8*, 3605–3612.